EXTENDED PDF FORMAT
SPONSORED BY
Announcing Enhanced Product Information Pages!
Evaluate our Data. Review Published Results.
Make a Confident Choice.
Learn more
R&D SYSTEMS
www.rndsystems.com/PSP

The Elemental Composition of Asteroid 433 Eros: Results of the NEAR-Shoemaker X-ray Spectrometer

J. I. Trombka *et al.*

Science **289**, 2101 (2000);
DOI: 10.1126/science.289.5487.2101

This copy is for your personal, non-commercial use only.

If you wish to distribute this article to others, you can order high-quality copies for your colleagues, clients, or customers by clicking here.

Permission to republish or repurpose articles or portions of articles can be obtained by following the guidelines here.

The following resources related to this article are available online at www.sciencemag.org (this information is current as of December 18, 2012):

Updated information and services, including high-resolution figures, can be found in the online version of this article at:
http://www.sciencemag.org/content/289/5487/2101.full.html

A list of selected additional articles on the Science Web sites **related to this article** can be found at:
http://www.sciencemag.org/content/289/5487/2101.full.html#related

This article has been **cited by** 59 article(s) on the ISI Web of Science

This article has been **cited by** 6 articles hosted by HighWire Press; see:
http://www.sciencemag.org/content/289/5487/2101.full.html#related-urls

Downloaded from www.sciencemag.org on December 18, 2012

Science (print ISSN 0036-8075; online ISSN 1095-9203) is published weekly, except the last week in December, by the American Association for the Advancement of Science, 1200 New York Avenue NW, Washington, DC 20005. Copyright 2000 by the American Association for the Advancement of Science; all rights reserved. The title *Science* is a registered trademark of AAAS.

iron chondrites (*29*), with measured densities of ~3200 to 3500 kg m−3 (*36*). Meteorite analogs are denser than Eros's bulk density, which suggests that the asteroid exhibits some degree of fracturing and/or porosity.
27. E. Asphaug, S. J. Ostro, R. S. Hudson, D. J. Scheeres, W. Benz, *Nature* **393**, 437 (1998).
28. A. Fujiwara *et al.*, in *Asteroids*, R. P. Binzel, T. Gehrels, M. S. Matthews, Eds. (Univ. of Arizona Press, Tucson, AZ, 1989), pp. 240–265.
29. J. Trombka *et al.*, *Science* **289**, 2101 (2000).
30. K. R. Housen and K. A. Holsapple, *Icarus* **84**, 226 (1990).
31. A. Fujiwara, *Icarus* **83**, 156 (1991).
32. Gravity was calculated from the shape model assuming homogeneous density. Centrifugal accelerations due to the asteroid's rotation were taken into account. The gravitational slope is the angle between $\vec{g}$ and $-\hat{n}$, the inward normal, as calculated from a plate representation of a 3° grid of NLR radii in which plates were characterized by areas that differed by up to a factor of 2.
33. A. Fujiwara, *Icarus* **89**, 384 (1991).
34. A. F. Cheng *et al.*, *Icarus*, in press.
35. O. Aharonson and M. T. Zuber, unpublished data.
36. G. J. Consolmagno and D. T. Britt, *Meteorit. Planet. Sci.* **33**, 1231 (1998).
37. D. D. Rowlands *et al.*, "GEODYN II System Description" (Hughes-STX Contractor Report, 1993).
38. J. J. McCarthy *et al.*, "GEODYN Systems Descriptions and Operations Manuals" (NASA Goddard Space Flight Center and Hughes/STX Contractor Report, 1994).
39. To determine the shape of Eros we used NLR data collected between days 065 and 190 of 2000 during spacecraft orbits with semi-axes (in km) as follows: 200 by 200, 100 by 200, 100 by 100, 100 by 50, and 50 by 50. We analyzed the NLR data in conjunction with the orbital ephemeris of NEAR and computed the orbit of the spacecraft using the GEODYN/SOLVE orbital analysis programs (*37*, *38*). We determined global topography from a joint inversion of altimetry and Doppler data, which yielded an altimetric model, spacecraft orbits, and a degree and order 5 gravity model, with coefficients through degree 3 given in Table 1. Using our orbits and gravity field and incorporating the pointing data from spacecraft quaternions that yield the attitude and orientation of the spacecraft in inertial space, we estimated the locations of bounce points of the laser pulse on the surface of Eros. Asteroid radii were measured by subtracting ranges from the spacecraft orbit.
40. We thank the NEAR-Shoemaker spacecraft, mission operations, and navigation teams for support. We also thank B. Williams and D. Yeomans for providing tracking data used to calculate the orbits, P. Thomas for helpful discussions, D. Pavlis and J. McCarthy for assistance in tracking data analysis, and M. Nolan for review. The NLR investigation is supported by the NASA NEAR-Shoemaker Project.

30 May 2000; accepted 30 August 2000

The Elemental Composition of Asteroid 433 Eros: Results of the NEAR-Shoemaker X-ray Spectrometer

J. I. Trombka,[1]* S. W. Squyres,[2] J. Brückner,[3] W. V. Boynton,[4] R. C. Reedy,[5] T. J. McCoy,[6] P. Gorenstein,[7] L. G. Evans,[8] J. R. Arnold,[9] R. D. Starr,[10] L. R. Nittler,[1] M. E. Murphy,[10] I. Mikheeva,[4] R. L. McNutt Jr.,[11] T. P. McClanahan,[1] E. McCartney,[2] J. O. Goldsten,[11] R. E. Gold,[11] S. R. Floyd,[1] P. E. Clark,[10] T. H. Burbine,[6] J. S. Bhangoo,[4] S. H. Bailey,[4] M. Petaev[7]

We report major element composition ratios for regions of the asteroid 433 Eros imaged during two solar flares and quiet sun conditions during the period of May to July 2000. Low aluminum abundances for all regions argue against global differentiation of Eros. Magnesium/silicon, aluminum/silicon, calcium/silicon, and iron/silicon ratios are best interpreted as a relatively primitive, chondritic composition. Marked depletions in sulfur and possible aluminum and calcium depletions, relative to ordinary chondrites, may represent signatures of limited partial melting or impact volatilization.

The Near Earth Asteroid Rendezvous (NEAR)–Shoemaker mission began an orbital rendezvous with the S-type asteroid Eros on 14 February 2000. The x-ray/gamma-ray spectrometer system (XGRS) on NEAR detects 1- to 10-keV x-rays and 0.3- to 10-MeV gamma-ray emissions. Discrete line x-ray and gamma-ray emissions in these energy domains can be used to determine the surface distribution of many geologically important elements (e.g., Mg, Al, Si, S, Ca, Fe, O, K, and possibly Th) (*1–3*). In addition, NEAR carries a near-infrared spectrometer and a multispectral imager (*4–6*), allowing direct comparison between the elemental composition measured by the XGRS and the mineralogy inferred from the optical and infrared spectral measurements. These complementary data sets will help elucidate possible relations to known classes of meteorites and processes that might have occurred on Eros (e.g., impact metamorphism and partial melting).

Since 2 May 2000, NEAR has been in a low (35- to 50-km) orbit about the center of mass of Eros, beginning an extended phase of detailed surface mapping of the asteroid. Here, we report results from the NEAR x-ray spectrometer (XRS) on the surface composition of Eros. These results are compared to compositions of meteorite groups. Statistically significant results from gamma-ray spectrometry require integration times that are substantially longer than those from x-ray spectrometry results.

Remote sensing x-ray spectroscopy. The x-ray spectrum of a planetary surface measured from orbit is dominantly a combination of the fluorescence excited by incident solar x-rays and coherently and incoherently scattered solar x-rays from the surface. The sampling depth is dependent on energy, but it is always less than 100 μm for the elements of interest here. The most prominent characteristic x-ray fluorescent lines that can be observed by the NEAR XRS are the Kα lines (1 to 10 keV) from the major elements Mg (1.254 keV), Al (1.487 keV), Si (1.740 keV), S (2.308 keV), Ca (3.691 keV), and Fe (6.403 keV). Emission produced by solar and cosmic charged particles is negligible, and astronomical x-ray sources are occulted by the asteroid, which fills the field of view below an altitude of 400 km.

Incident solar x-rays provide the excitation source for x-ray generation from a planetary surface. Thus, knowledge of the solar spectrum is critical to obtaining quantitative analyses (*7, 8*). The solar flux from 1 to 10 keV is composed of a continuum and discrete lines. Theoretical models predict the solar spectrum as a function of solar activity (*9–12*). Solar intensity decreases by three to four orders of magnitude from 1 to 10 keV, so fluorescent lines and scatter-induced background radiation exhibit greater intensity at lower energies. As solar activity increases, the spectra harden, with increased output at higher energies, reduced steepness in the spectral slope, and increased overall x-ray

[1]Goddard Space Flight Center, Code 691, Greenbelt, MD 20771, USA. [2]Space Sciences Building, Cornell University, Ithaca, NY 14853, USA. [3]Max-Planck-Institut für Chemie, Postfach 3060, D-55020 Mainz, Germany. [4]Department of Planetary Science, Space Sciences Building, University of Arizona, Tucson, AZ 85721, USA. [5]Los Alamos National Laboratory, NIS-2, MS-D436, Los Alamos, NM 87545, USA. [6]Department of Mineral Sciences, National Museum of Natural History, Smithsonian Institution, Washington, DC 20560–0119, USA. [7]Smithsonian Astrophysical Observatory, 60 Garden Street, MS-4, Cambridge, MA 02138, USA. [8]System Sciences Division, Computer Sciences Corporation, 1100 West Street, Laurel, MD 20707, USA. [9]University of California, San Diego, Chemistry BC-017/Cal Space 0524, 9500 Gillman Drive, La Jolla, CA 92093, USA. [10]Physics Department, Catholic University of America, 620 Michigan Avenue NE, Washington, DC 20064, USA. [11]Applied Physics Laboratory, Johns Hopkins University, Johns Hopkins Road, Laurel, MD 20723, USA.

*To whom correspondence should be addressed.

Downloaded from www.sciencemag.org on December 18, 2012

flux. Solar output is highly variable and can change one to four orders of magnitude over time spans of minutes to hours, respectively, and must be monitored continuously. Higher solar activity produces a higher incident x-ray flux and, thus, greater excitation from the surface, particularly for heavy elements (e.g., Fe). This increased flux allows shorter integration times with better signal-to-noise ratios, increased statistical accuracy, and finer spatial resolution maps.

NEAR XRS detectors. The asteroid-pointing XRS detector package includes three large-area (25 cm^2) sealed gas proportional counters with thin Be windows (*13, 14*). A collimator (a honeycomb of Cu with 3% Be) is used to increase spatial resolution for asteroid mapping and to reduce the sky background. A 5° full field of view yields an optimal spatial resolution of ~4.4 km at a distance of 50 km from the surface of the asteroid. The energy resolution of these detectors measured in the laboratory and in flight is ~14% at 5.9 keV. The proportional counters do not have the energy-resolving power to separate the lower energy Mg, Al, and Si lines.

For the separation of the Mg, Al, and Si lines, an Apollo-style balanced filter system is used (*1, 2, 7, 8, 13, 14*). The three proportional counters are differentially filtered, with one unfiltered detector, one detector with a Mg filter, and the third with an Al filter. The unfiltered detector system allows all three lines to pass into the detector without substantial alteration. The Mg filter detector system strongly absorbs the Al and Si lines but allows an attenuated Mg signal to be clearly defined. The Al filter detector system allows for the measurement of attenuated Mg and Al lines but completely absorbs the Si line. From an analysis of these three spectra, the intensity of the three lines can be uniquely determined. An additional gas proportional counter detector, similar to the ones described above, is oriented at 90° from the asteroid-pointing detectors and monitors the sun. This detector has a graded shield filter specially designed to enhance its sensitivity at high energies where the solar flux is low (*3*). The primary source of background in the four detectors is galactic cosmic-ray interactions with the gas. A rise-time discrimination circuit is used to reduce this background above 3 keV.

Calibration and analysis methods. Between 2 May and 25 July 2000, while the NEAR spacecraft was in 50- and 35-km orbits around the center of mass of Eros, Geostationary Operational Environmental Satellites (GOES) and the XRS solar monitor detected more than 80 M-class and higher solar flares. Of these, ~30 produced measurable fluorescence from the asteroid's surface. We present analyses of two of the larger events, from 4 May and 19 July, for which statistically significant spectra were obtained. In addition, results for quiet sun spectra collected over the period from 2 May to 7 July are presented (*15*) (Table 1).

The regions of Eros observed by XRS during the flare and quiet sun measurements, hereafter referred to as "footprints" (Fig. 1), are concentrated in the northern hemisphere because the sun did not pass south of Eros' equator until 25 June. Spacecraft-pointing restrictions and the unusual geometry of Eros are responsible for the uneven coverage. The quiet sun spectra are concentrated around the 5-km

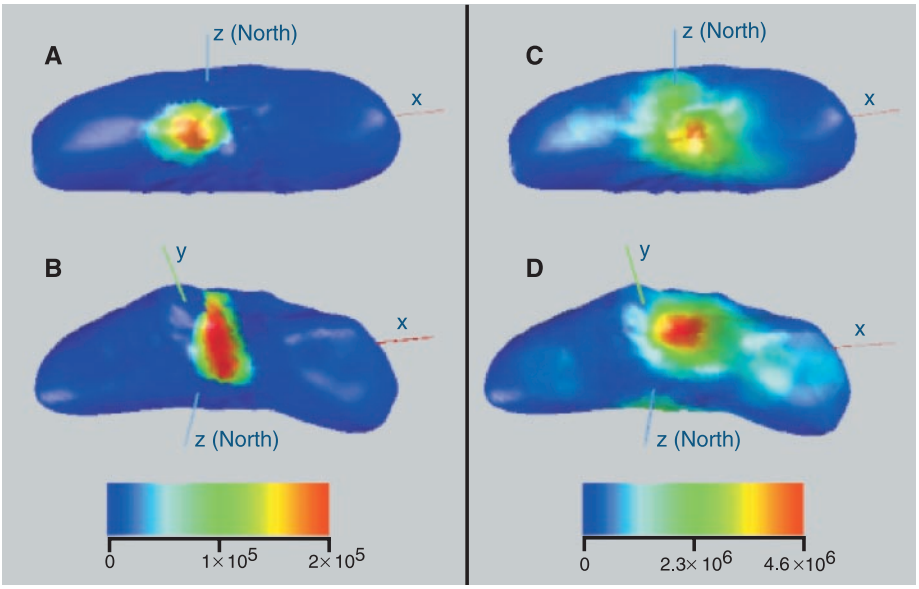

Fig. 1. Footprints projected onto the plate model of Eros (*31*) for areas observed during solar flares on (**A**) 4 May 2000 and (**B**) 19 July 2000. Accumulated footprints during periods of quiet sun from 2 May to 7 July 2000 are projected onto the model in (**C**) and (**D**) for the same areas observed as in (A) and (B), respectively. Quiet sun coverage is concentrated in the crater Psyche (C) and the "saddle" region Himeros (D). The color scale represents valid events in the unfiltered asteroid-pointing detector.

Table 1. Basic data for quiet sun integration and two solar flares.

Spectrum	Total integration time (s)	Latitude (degrees)	Longitude (degrees)	Average solar plasma temperature (10^6 K)
Quiet sun	2.729×10^5	—	—	4.6
4 May flare	1400	13	148	16
19 July flare	1450	46	−61	13

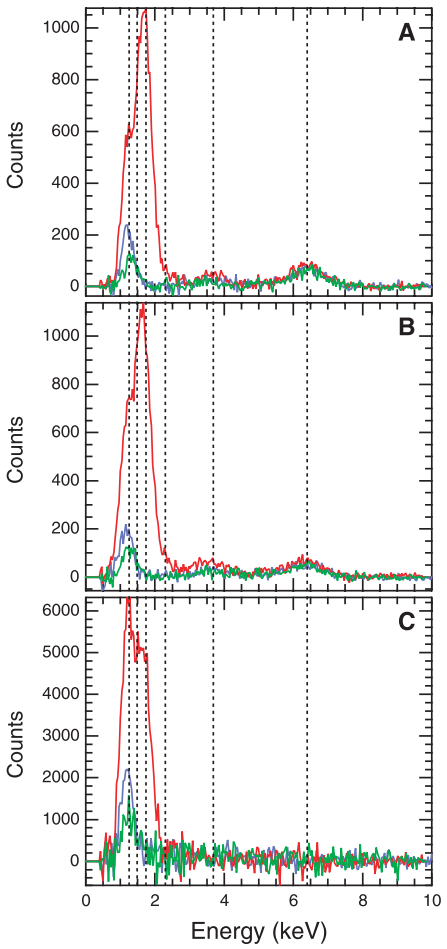

Fig. 2. X-ray emission spectra obtained with the three Eros-pointed x-ray detectors (red, unfiltered; blue, Mg filtered; and green, Al filtered) during (**A**) a solar flare on 4 May 2000, (**B**) a solar flare on 17 July 2000, and (**C**) the quiet sun period from 2 May to 7 July 2000. Vertical lines indicate positions of Kα lines of Mg (1.254 keV), Al (1.487 keV), Si (1.740 keV), S (2.308 keV), Ca (3.691 keV), and Fe (6.403 keV).

Downloaded from www.sciencemag.org on December 18, 2012

crater Psyche and the large saddle named Himeros. The footprint of the 4 May flare is centered just outside and to the west of Psyche. The 19 July flare footprint centers on the northern portion of the saddle Himeros but extends across much of this feature.

Background-subtracted spectra for the two flares and the quiet sun data (Fig. 2) show two important differences between the flare spectra and the quiet sun spectrum. First, the flare spectra contain fluorescence from the higher energy S, Ca, and Fe lines, whereas the quiet sun spectrum does not. Second, the lower energy Mg line is enhanced with respect to the Si line in the quiet sun spectrum. In both cases, this reflects the much harder solar x-ray spectrum produced during flares. Converting XRS spectra to elemental abundances requires that detector background be accurately removed and that x-ray line intensities for the various elements be determined. Background varies by several percent in absolute count rate on a time scale of days to weeks. Variations in spectral shape are smaller but significant for low signal-to-noise ratio data (e.g., the quiet sun spectrum). The background shape is determined from spectra obtained while observing the asteroid's dark side and normalized to the fluorescence spectra. Once background is subtracted, x-ray line fluxes are determined by a combination of matrix deconvolution of the three balanced-filter spectra to obtain Mg, Al, and Si fluxes (*7, 8, 16, 17*) and curve fitting to Gaussian peak shapes to obtain S, Ca, and Fe fluxes. Derived detector count rates are corrected for detector efficiencies to obtain incident photon fluxes for each element.

Here, we consider elemental ratios rather than absolute abundances, because ratioing eliminates many geometrical factors affecting the production and scatter of x-rays (*16, 17*). We ratio abundances to Si, because it fluoresces under quiet sun and solar flare conditions and because its x-ray line lies between the two other most abundant observable rock-forming elements, Mg and Fe (Table 2).

Solar temperatures, which are critical for converting photon ratios to elemental abundance ratios, are derived from x-ray fluxes measured by the GOES spacecraft. During May through July 2000, NEAR and GOES viewed the same portion of the sun. GOES fluxes and NEAR solar monitor count rates were also seen to track consistently during this time period. Reliable techniques to calculate temperature from GOES data have been given by Thomas *et al.* (*18*) and Garcia (*19*). We used the model of Garcia (*19*) to derive weighted average temperatures for our three integrations (Table 1).

With the derived photon ratios and solar temperatures, the relative elemental abundances can be calculated (Table 2). We used an analytic model, similar to that described by Jenkins and DeVries (*20*), to predict fluorescent and scattered x-ray spectra for any assumed elemental composition, incident solar spectrum, and observational geometry (*21*). We used the absorption coefficients of Henke *et al.* (*22*) and a scattering model derived from work by Compton and Allison (*23*). The scattered spectrum is relatively insensitive to elemental composition. The assumed solar x-ray spectra are based on the model of Raymond and Smith (*12*). The validity of such models has been previously confirmed by the analysis of lunar x-ray spectra from Apollo 15 and 16 (*7, 8, 13, 14, 16*). We calculated model spectra for seven meteorite compositions, corresponding to a wide range of meteorite types, for eight solar plasma temperatures from 4 million to 40 million kelvin. From these models, we derived calibration curves relating predicted photon ratios (fluorescence plus scatter) to element concentration ratios for each solar temperature. Calibration curves for intermediate temperatures are interpolated from these calculations (Fig. 3).

Errors reported for elemental ratios from the two flare and quiet sun spectra are for counting statistics only. Other possible sources of uncertainty are due to an imprecise knowledge of the background spectra and solar temperature and possible errors in the modeling. Of these, we suggest that errors related to solar temperature and modeling are relatively minor. The largest source of error results from a lack of knowledge of the magnitude and shape of the background spectra. This error most seriously affects the derived Mg/Si and Al/Si ratios. Because the 19

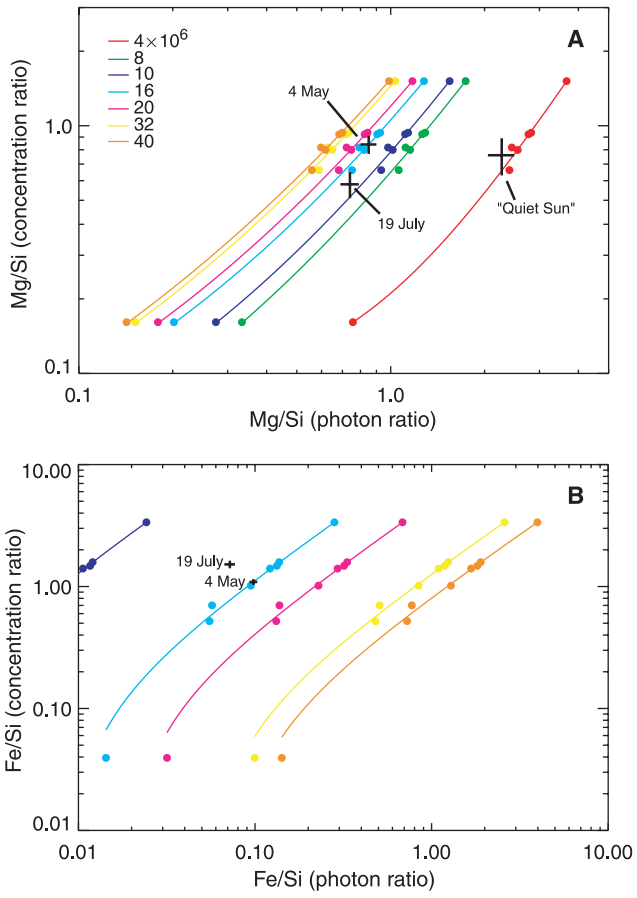

Fig. 3. Theoretical calibration curves relating x-ray photon ratios to concentration ratios for (**A**) Mg/Si and (**B**) Fe/Si, for a range of solar temperatures (at 10^6 K). Solid circles are results of model calculations for specific meteorite compositions; solid curves are second-order polynomial fits to the points. Each set of colored points and curve corresponds to the indicated solar temperature. Error bars indicate results from the quiet sun spectrum and two solar flare spectra interpolated to derived solar temperatures (Table 1). Mg/Si photon ratios decrease and Fe/Si ratios increase with increasing solar temperature, reflecting the spectral hardening of the solar x-ray spectrum with temperature. Similar calibration curves were used to derive Al/Si and Ca/Si ratios. The measured S/Si photon ratios (Table 2) are lower than the predicted ratios for any S/Si concentration ratio for the flare temperatures, and we hence report upper limits for this elemental ratio in Table 2.

Table 2. Derived photon and elemental abundance ratio data for Eros from quiet sun integration and two solar flares. Elemental ratios are by weight. Quoted uncertainties are due to counting statistics and do not include a possible systematic uncertainty due to changing background shape.

Spectrum	Ratio	Mg/Si	Al/Si	S/Si	Ca/Si	Fe/Si
Quiet sun	Photon	2.27 ± 0.22	0.22 ± 0.11	—	—	—
	Elemental	0.76 ± 0.13	0.06 ± 0.06	—	—	—
4 May flare	Photon	0.85 ± 0.05	0.06 ± 0.03	0.036 ± 0.007	0.056 ± 0.014	0.098 ± 0.005
	Elemental	0.84 ± 0.07	0.02 ± 0.03	<0.01	0.056 ± 0.006	1.09 ± 0.06
19 July flare	Photon	0.74 ± 0.05	0.10 ± 0.03	0.052 ± 0.006	0.070 ± 0.006	0.072 ± 0.005
	Elemental	0.59 ± 0.05	0.06 ± 0.03	<0.01	0.081 ± 0.009	1.52 ± 0.11

Downloaded from www.sciencemag.org on December 18, 2012

July flare occurred shortly after a major solar particle event, resulting in a highly variable background throughout the day, derived Mg/Si and Al/Si ratios for this event may have particularly large errors from background derivation, perhaps as much as 30%.

Data interpretation. Two of the major goals of the NEAR mission to Eros are linking this asteroid to known groups of meteorites and deciphering the processes that led to the formation of this asteroid. We compared the derived major element composition ratios (Mg, Al, S, Ca, and Fe, ratioed to Si) from Eros with bulk compositions of known meteorites using a database we designed for this purpose (Fig. 4) (*24, 25*) to determine whether the composition of Eros is similar to that of any known meteorite group.

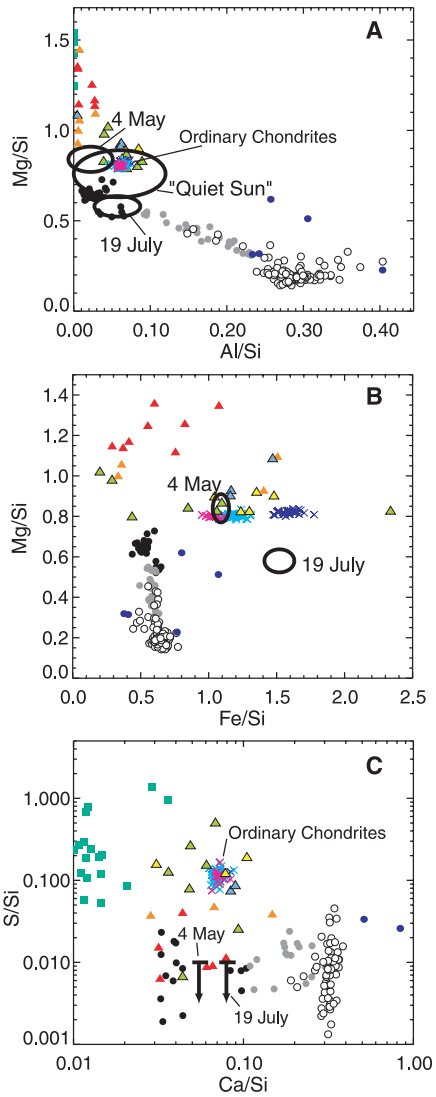

Fig. 4. Elemental ratios derived for Eros (1σ error ellipses) for the quiet sun period from 2 May to 7 July 2000 and two solar flares (4 May and 19 July 2000). For comparison, laboratory data of likely meteorite analogs are plotted as well. Ordinary chondrites are plotted as crosses (dark blue, H; light blue, L; and pink, LL). Primitive achondrites are shown as triangles (yellow, acapulcoites; orange, lodranites; green, winonaites; red, ureilites; and blue, brachinites). Achondrites are plotted as circles (black, diogenites; white, eucrites; gray, howardites; and dark blue, angrites). Pallasites are plotted as green squares. Meteorite data are taken from a large database of meteorite compositions (*24, 25*). (**A**) Mg/Si versus Al/Si, (**B**) Mg/Si versus Fe/Si, and (**C**) Ca/Si versus S/Si. Pallasites are off scale on (B); downward arrows in (C) represent upper limits on S/Si.

A first-order question in the study of Eros is whether this asteroid has experienced global differentiation or retains a primitive chondritic composition. The abundances of Al, Mg, and Si are particularly diagnostic for this purpose because Al strongly partitions into early partial melts, leaving Mg-enriched residues. Al-rich compositions are absent from the areas sampled during the 4 May and 19 July flares and the quiet sun spectrum. The howardite-eucrite-diogenite suite of meteorites is pyroxenitic to basaltic rocks thought to represent partial melts and complementary fractional crystallization products. These meteorites best sample the surficial layer of an asteroid that has differentiated into a core, mantle, and crust (*26*). In contrast to the Al-rich compositions found in this suite, the regions of Eros analyzed here are similar to the unfractionated H, L, and LL ordinary chondrites in their low Al/Si ratios. In fact, these areas could be depleted in Al, relative to ordinary chondrites, although current uncertainties are too large to determine this with confidence. Mg/Si ratios for the quiet sun and 4 May flare overlap with the ratios for ordinary chondrites. The 19 July flare footprint has apparently lower Mg/Si than ordinary chondrites, within the range for diogenites. We doubt, however, that Eros contains a diogenitic lithology, given the lack of expected, complementary Al-rich lithologies and the incompatible inferred history of primitive, chondritic material and differentiated diogenite material. We conclude that Eros has not experienced global differentiation.

Fe, a major rock-forming element, is readily fractionated by a range of geologic processes and has been used extensively to distinguish between different classes of meteorites (*27*). The quiet sun spectrum does not exhibit Fe fluorescence and is not plotted. The Fe/Si ratios of the two flare footprints bracket those of the ordinary chondrites, as well as several groups of meteorites that have experienced limited degrees of partial melting during their formation [e.g., primitive achondrites (Fig. 4B)]. Given possible nonstatistical errors discussed earlier, we favor a conservative interpretation that Eros is undifferentiated and the Fe/Si and Mg/Si ratios of the two flare footprints may be identical. The alternative, that these differences point to global heterogeneity, would probably require some limited differentiation and cannot be ruled out.

S and Ca can be particularly diagnostic of low degrees of melting because they are concentrated in early partial melts (*28*). The two flare regions are depleted in S, relative to ordinary chondrites (Fig. 4C). The Ca/Si ratios are similar to those of ordinary chondrites, although a slight Ca depletion is hinted by the 4 May flare. The depletion of S has several possible interpretations. It could be a primary feature of the chondritic material that accreted to form Eros. This seems unlikely because the S/Si ratios for the plotted ordinary chondrites, already the lowest of any measured unweathered chondritic meteorites (*24, 25*), are an order of magnitude greater than that inferred for Eros. Alternatively, the low S abundance could point to limited melting and differentiation. The first partial melt to form in a chondritic system is at the Fe,Ni-FeS cotectic and contains ~85 weight % FeS or ~30 weight % S (*29*). Removal of this melt could produce substantial S depletions. In the meteoritic record, however, such S depletions are accompanied by silicate melting and depletions in elements (e.g., Al, Ca, and K) concentrated into early silicate partial melts. Although Al and Ca depletions cannot be ruled out by our data, the results are ambiguous. Finally, the depletion of S may only occur in the top few hundred micrometers of the regolith sampled by x-rays and may be a consequence of impact bombardment. S is a volatile element, and impact vaporization and disassociation of troilite (FeS) found in ordinary chondrites could produce S depletions (*30*).

References and Notes

1. J. I. Trombka *et al.*, *J. Geophys. Res.* **102**, 23729 (1997).
2. J. O. Goldsten *et al.*, *Space Sci. Rev.* **82**, 169 (1997).
3. P. E. Clark, S. R. Floyd, J. I. Trombka, *NASA Conf. Publ.* **NASA CP-3353**, 31 (1997).
4. J. Veverka *et al.*, *J. Geophys. Res.* **102**, 23709 (1997).
5. S. E. Hawkins III *et al.*, *Space Sci. Rev.* **82**, 31 (1997).
6. J. W. Warren *et al.*, *Space Sci. Rev.* **82**, 101 (1997).
7. P. E. Clark, thesis, University of Maryland, College Park (1979).
8. _____ and J. I. Trombka, *J. Geophys. Res.* **102**, 16361 (1997).
9. W. H. Tucker and M. Koren, *Astrophys. J.* **168**, 283 (1971).
10. R. Mewe, *Sol. Phys.* **22**, 459 (1972).
11. R. Kreplin, K. Dere, D. Horan, J. Meekin, in *Solar Output and Its Variation* (Associated University Press, Boulder, CO, 1977), pp. 287–312.
12. J. C. Raymond and B. W. Smith, *Astrophys. J. Suppl. Ser.* **35**, 419 (1977).
13. I. Adler, J. I. Trombka, P. Gorenstein, *Anal. Chem.* **44**, 28A (1972).
14. C. Fichtel and J. I. Trombka, *NASA Ref. Publ.* **1386**, 1 (1997).
15. We define quiet sun data as those spectra that are collected while the solar monitor event rate is less than 300 counts per second. This event rate corresponds to a high B- to low C-level solar x-ray output as measured by the GOES spacecraft. A B-level flare produces a flux of 10^{-7} to 10^{-6} W m^{-2} in the GOES 0.1- to 0.8-nm-wavelength detector; the C level flux is 10^{-6} to 10^{-5} W m^{-2}. For comparison, at the peak of the two flares (M level, 10^{-5} to 10^{-4} W m^{-2}), the solar monitor rate exceeded 7500 counts per second.
16. J. I. Trombka, J. R. Arnold, I. Adler, A. E. Metzger, R. C. Reedy, *NASA Spec. Publ.* **NASA SP-370**, 153 (1977).
17. J. I. Trombka *et al.*, *Computers in Activation Analysis and Gamma-ray Spectroscopy*, *Conf. 780421* (National Technical Information Service, U.S. Department of Commerce, Springfield, VA, 1979), p. 26.

Downloaded from www.sciencemag.org on December 18, 2012

18. R. J. Thomas, R. Starr, C. J. Crannell, *Sol. Phys.* **95**, 323 (1985).
19. H. A. Garcia, *Sol. Phys.* **154**, 275 (1994).
20. R. Jenkins and J. DeVries, *Practical X-ray Spectrometry* (Springer-Verlag, New York, 1967).
21. P. Gorenstein, H. Gursky, G. Garmire, *Astrophys. J.* **153**, 885 (1968).
22. B. L. Henke, E. M. Gullikson, J. C. Davis, *At. Data Nucl. Data Tables* **54**, 181 (1993).
23. A. H. Compton and S. K. Allison, *X-rays in Theory and Experiment* (Van Nostrand, Princeton, NJ, 1935), appendix IV.
24. L. R. Nittler, P. E. Clark, T. J. McCoy, M. E. Murphy, J. I. Trombka, in *Asteroids, Comets, Meteors '99* (1999).
25. _____, *Lunar Planet. Sci. Conf.* **XXXI**, abstract 1711 (2000) [CD-ROM].
26. D. W. Mittlefehldt, T. J. McCoy, C. A. Goodrich, A. Kracher, in *Planetary Materials,* J. J. Papike, Ed. (Mineralogical Society of America, Washington, DC, 1998), pp. 41–195.
27. H. C. Urey and H. Craig, *Geochim. Cosmochim. Acta* **4**, 36 (1953).
28. T. J. McCoy *et al.*, *Icarus*, in press.
29. G. Kullerud, *Annu. Rep. Geophys. Lab.* **67**, 4055 (1963).
30. A. E. Rubin and S. Arnold, *Meteorit. Planet. Sci.* **35** (suppl.), A138 (2000).
31. T. P. McClanahan *et al.*, *Nucl. Instrum. Methods Phys. Res. A* **422**, 582 (1999).
32. We thank the NEAR project offices at Johns Hopkins University/Applied Physics Laboratory (JHU/APL) and NASA Headquarters. The NEAR mission is supported by NASA Task 005 NASA contract NAS 5-97271, by NASA contract 624-03-03, and by the Planetary Instrument Definition and Development Program under NASA contract 344-96-30. The XGRS Team also recognizes the exemplary efforts of the NEAR Mission Operations Team and the NEAR Science Data Center at JHU/APL for enabling the collection of the data that have made this analysis possible. We thank the student support at Cornell University, the University of Arizona, and Goddard Space Flight Center. The contributions of P. Solomon are greatly appreciated. We would particularly like to acknowledge the late Isidore Adler, a pioneer in establishing x-ray remote sensing for planetary geochemical exploration and the late Jurgen Rahe, an unwavering supporter of the NEAR mission.

17 August 2000; accepted 28 August 2000

The Kondo Effect in the Unitary Limit

W. G. van der Wiel,[1]* S. De Franceschi,[1] T. Fujisawa,[2] J. M. Elzerman,[1] S. Tarucha,[2,3] L. P. Kouwenhoven[1]

We observe a strong Kondo effect in a semiconductor quantum dot when a small magnetic field is applied. The Coulomb blockade for electron tunneling is overcome completely by the Kondo effect, and the conductance reaches the unitary limit value. We compare the experimental Kondo temperature with the theoretical predictions for the spin-1/2 Anderson impurity model. Excellent agreement is found throughout the Kondo regime. Phase coherence is preserved when a Kondo quantum dot is included in one of the arms of an Aharonov-Bohm ring structure, and the phase behavior differs from previous results on a non-Kondo dot.

The Kondo theory explains the increased resistivity of a metal with magnetic impurities at low temperatures (*1*). Predictions from 1988 indicate that quantum dots could also exhibit the Kondo effect (*2–7*) as an increased conductance G, which can reach the unitary limit ($G = 2e^2/h$, where e is the electronic charge and h is Planck's constant) at low temperature. Recent experiments have confirmed the presence of the Kondo effect in quantum dots; however, the unitary limit was not reached (*8–12*). We demonstrate the unitary limit Kondo effect in a semiconductor quantum dot. Our quantum dot is embedded in one of the arms of an Aharonov-Bohm (AB) ring, which enables us to show that electron transport through the many-body Kondo state is at least partly phase coherent.

The Kondo effect arises from the coupling between a localized electron spin and a sea of conduction electrons. The strength is characterized by the Kondo temperature T_K (*13*)

$$T_K = \frac{\sqrt{\Gamma U}}{2} e^{\pi\varepsilon_0(\varepsilon_0 + U)/\Gamma U} \quad (1)$$

U is the on-site electron repulsion energy, or charging energy; ε_0 is the energy of the single-particle state; and Γ reflects its width, due to a finite lifetime from tunneling to the leads. In quantum dots, these parameters can be controlled experimentally, resulting in a "tunable Kondo effect" (*8–12*).

Our device (Fig. 1A) consists of an AB ring defined in a two-dimensional electron gas (2DEG) (*14*). The conductance of the ring without applying gate voltages is $\sim 10e^2/h$, implying that the current is carried by several modes in each arm. In our experiment, a quantum dot has only been formed in the lower arm. One gate in the upper arm is used to pinch off the upper arm. All measurements are performed in a dilution refrigerator with a base temperature of 15 mK, using a standard lock-in technique with an ac voltage excitation between source and drain contacts of 3 μV.

The linear-response conductance G through the lower dot versus gate voltage V_{gl} and magnetic field B is shown in Fig. 1B. Here, the left and right parts of the lower arm serve as leads to the dot. In Fig. 1C, two $G(V_{gl})$ curves are extracted from Fig. 1B for $B = 0$ and 0.4 T. At $B = 0$, regular Coulomb oscillations are observed with low valley conductance. In some magnetic field ranges, however, the valley conductance increases considerably and can even reach $2e^2/h$ (for instance, for $B = 0.4$ T). Figure 1B is discussed in more detail below, but first, we focus on the large conductance values observed at $B = 0.4$ T.

Figure 2A shows Coulomb oscillations for different temperatures. At the base temperature, the valleys around $V_{gl} = -413$ and -372 mV reach the maximum possible conductance value of $2e^2/h$. In fact, the valleys tend to disappear. When the temperature is increased, two separate Coulomb peaks develop with growing peak spacing. The conductance in the center of the valley has a logarithmic T dependence with a saturation at $2e^2/h$ for low T, which is not due to electronic noise (Fig. 2A, right inset). The adjacent Coulomb valleys show an opposite T dependence. This even-odd asymmetry indicates an unpaired spin in a valley with an odd electron number, where we observe the Kondo anomaly, and a spin singlet for an even electron number (*8, 9*). Figure 2B shows the differential conductance for different T values in the middle of the Kondo plateau at $2e^2/h$. The pronounced peak around $V_{SD} = 0$ reflects the Kondo resonance at the Fermi energy (V_{SD} is the dc bias voltage between source and drain contacts). The peak height has the same T dependence as shown in Fig. 2A, right inset. The width of the peak increases linearly with temperature (Fig. 2B, inset).

These measurements are taken after optimizing the two barrier gate voltages, V_{gl} and V_{gr}, to obtain nearly equal tunnel barriers. However, sweeping V_{gl}, as in Fig. 2A, changes the left barrier much more effectively than the right tunnel barrier, and hence the barriers cannot be symmetric over the whole V_{gl} range. For a quantitative comparison to theory, we therefore optimize V_{gr} by fixing it at a value chosen such that, upon sweeping V_{gl}, we obtain a flat plateau close to $2e^2/h$ (Fig. 3A) (*15*). The two discernable Coulomb oscillations at higher temperatures have completely merged together at low temperature. This unitary limit was predicted (*3, 4*) but not observed before. The unitary limit implies that the transmission probability through the quantum dot is equal to one. This is a remarkable phenomenon because the quantum dot contains two tunnel barriers, each with a

[1]Department of Applied Physics, Delft Institute for Microelectronics and Submicrontechnology, and ERATO Mesoscopic Correlation Project, Delft University of Technology, Post Office Box 5046, 2600 GA Delft, Netherlands. [2]NTT Basic Research Laboratories, Atsugi-shi, Kanagawa 243–0198, Japan. [3]ERATO Mesoscopic Correlation Project, University of Tokyo, Bunkyo-ku, Tokyo 113–0033, Japan.

*To whom correspondence should be addressed. E-mail: wilfred@qt.tn.tudelft.nl

Downloaded from www.sciencemag.org on December 18, 2012